Received: 27 August 2020 | Revised: 25 November 2020 | Accepted: 12 December 2020

DOI: 10.1002/eqe.3413

RESEARCH ARTICLE

WILEY

Variability of near-fault seismic risk to reinforced concrete buildings based on high-resolution physics-based ground motion simulations

Maha Kenawy[1] | **David McCallen**[1,2] | **Arben Pitarka**[3]

[1] Department of Civil and Environmental Engineering, University of Nevada, Reno, Nevada, USA

[2] Earth and Environmental Sciences, Lawrence Berkeley National Laboratory, California, USA

[3] Atmospheric, Earth and Energy Division, Lawrence Livermore National Laboratory, California, USA

Correspondence
Maha Kenawy, Department of Civil and Environmental Engineering, University of Nevada, Reno, 1664 N. Virginia Street, Reno, NV 89557, USA.
Email: mkenawy@unr.edu

Funding information
U.S. Department of Energy, Grant/Award Number: 17-SC-20-SC

Abstract

Broadband physics-based simulated earthquake ground motions are utilized to characterize the regional-scale seismic risk to modern reinforced concrete (RC) structures. A highly dense dataset of ground motions covering a 100-km × 40-km domain was generated using kinematic fault rupture models with varying rupture characteristics to represent shallow crustal earthquakes and resolved up to frequencies of 5 Hz. Over 40,000 nonlinear response history simulations of short- and mid-rise RC special moment frame buildings were conducted using simulation models that are capable of representing nonlinear behavior and component deterioration effects. The spatial variability of structural risk within a single earthquake scenario and between different rupture scenarios is examined, and the regions of strongest directivity effects and highest structural demands are identified. The structural demands may vary by factor of up to 8.0 at very short distances from the fault, and the large dispersion in the demands decreases significantly beyond a distance of 15 km. The interstory drift and member rotation demands are substantially impacted by important features of the geological structure and the characteristics of the rupture scenarios, particularly the presence of localized high-slip regions. The frequency characteristics of the structures are found to play an important role in determining the effects of near-fault ground motions on the structural response and expected damage. The results of this study suggest that the simulated ground motions, particularly those generated using the hybrid rupture approach, may offer reasonable structural risk estimates for low-frequency structures and conservative estimates for high-frequency structures.

KEYWORDS

forward directivity, ground motion simulations, regional-scale risk, reinforced concrete, shallow basin

1 | INTRODUCTION AND BACKGROUND

Characterizing the complex variability of risk to engineered structures near active earthquake faults is a challenging problem hindered by the sparsity of observed earthquake ground motion data in the near-source region. Ground motions

within about 15 km from rupturing faults exhibit unique characteristics that are different from shaking recorded at long distances. These near-fault ground motions can contain strong velocity pulses, which result from propagation of the fault rupture front at a speed close to the local shear wave velocity. When the rupture propagates toward a site in a strike-slip faulting mechanism, the site may experience the concentration of the seismic energy in one large pulse at the beginning of the shaking, which can cause severe damage to structures. This effect is known as forward directivity and has been observed near rupturing faults as early as the 1966 Parkfield, CA, earthquake[1] and the 1971 San Fernardo, CA, earthquake, during which extensive damage to flexible structures was attributed to the poorly understood effects of pulse-type ground motions.[2] The strength and deformation demands imposed on structures located near earthquake faults began to receive significant attention from engineers following the observed structural damage in the 1992 Landers, 1994 Northridge, and 1995 Kobe earthquakes.[3–5] This attention was necessitated by the fact that code provisions were historically developed based on recorded far-field ground motions, but progress was stymied by the limited number of available near-fault records.

The 1997 Uniform Building Code[6] contained a set of amplification factors for standard design spectra for sites located near active faults. These factors were later deemed inadequate in providing consistent protection to structures, because they did not consider the unique characteristics of near-fault ground motions.[5] ASCE 7-16,[7] one of the key documents adopted for building design in the United States, establishes restrictive design criteria for near-fault sites and requires consideration of near-fault motion characteristics in the selection and scaling of ground motion records for nonlinear response history analysis. In most engineering applications, selection of earthquake ground motions is performed with the aide of empirically based ground motion prediction equations (GMPEs), which predict selected ground motion intensity parameters as a function of earthquake magnitude, distance, faulting, and path and site parameters. To account for forward directivity effects in engineering analysis, several researchers[8–10] developed modification factors to GMPEs based on empirical analysis of available near-fault data and characterization of fault-site geometry, and the effects of rupture directivity were later incorporated into probabilistic seismic hazard analysis.[11] Because GMPEs are calibrated using observations of past earthquakes, they can be deficient in predicting rare events (e.g., large magnitudes at short distances). Moreover, near-source ground motion is known to be substantially affected by source parameters; for example, the hypocenter location, rupture velocity, slip distribution over the fault, seismic wave propagation, and coupling of source radiation with geologic structure such as the amplification of waves by sedimentary basins. These are aspects that are difficult to account for in empirical models. Therefore, GMPEs contain large epistemic uncertainty and do not capture the variability seen at short distances. Because the response of engineered structures in the near-fault region is influenced heavily by the nature of the ground motion, these deficiencies are at odds with performance-based seismic design, which necessitates a detailed quantitative understanding of the response of structures to expected ground shaking.

In recent years, physics-based numerical simulation of earthquake ground motions has steadily emerged as an alternative to the use of empirical ground motion models (see Douglas and Aochi[12] for a review of different simulation approaches dating back to the 1970s). Physics-based fault rupture simulation methods have been evolving rapidly due to advances in understanding of earthquake rupture processes, computational model sophistication, and computing technologies. The use of simulated ground motions to analyze the response of structures to earthquake events has been the subject of several studies.[13–19] As the confidence in using synthetic ground motions in engineering applications has increased, more studies have focused on exploring the structural demands imposed by simulated near-fault ground motion during large earthquakes and at short distances.[20] The majority of studies in the literature utilize a hybrid simulation approach combining deterministic simulation at low frequencies and a stochastic simulation approach at the higher frequencies. Validation studies have demonstrated that the hybrid simulation approaches carry realistic features that are important for computing the response of different types of structures.[17,19,21,22] However, such approaches do not include the effects of wave propagation in three-dimensional (3D) earth models across a broad frequency band and may misrepresent the spectral correlation properties of ground motions at higher frequencies, which are important for structural risk assessments.[23,24]

Deterministic broadband 3D ground motion simulations are an attractive methodology to understand the site-specific variation of earthquake hazard because they can take into account the fault geometry and the physics of wave propagation. These types of simulations have the potential to provide a wealth of high-resolution ground motion datasets; however, they require a substantial computational effort to cover large regional domains with the discretization granularity required to simulate frequencies of engineering interest. Such computationally intensive simulations are becoming more feasible owing to the tremendous strides in high-performance computing (HPC) tools in recent years. In this study, we compute broadband (0–5 Hz) ground motions for a canonical 3D basin model using a fully deterministic wave propagation modeling approach, and the kinematic rupture generator of Graves and Pitarka.[25] We utilize the highly dense simulated ground motion dataset to characterize the regional-scale variation of risk to low- and mid-rise modern reinforced concrete (RC)

TABLE 1 Design properties of the RC buildings

Property	Twelve-story building	Three-story building
Number of bays	4	4
Bay width (ft)	20	24
Typical story height (ft)	13	13
First story height (ft)	18	18
Beam dimensions (inches)	20 × 30	22 × 32
Column dimensions (inches)	30 × 30	28 × 28
Seismic base shear coefficient	0.0758	0.1435
First-mode period (s)	2.23	0.75

buildings subjected to shallow crustal earthquakes. The ground motion simulations are generated as part of the EQSIM (Earthquake Simulation Framework for Physics-Based Fault-to-Structure Simulations) application development under the U.S. Department of Energy Exascale Computing Project,[26,27] and employ HPC to span a 100-km × 40-km regional-scale domain and resolve frequencies up to 5 Hz. The structural models of the buildings are capable of simulating the expected nonlinear behavior, including strength and stiffness degradation, of reinforced concrete frames up to collapse. The objectives of this study are (1) to characterize the spatial variability of the structural demands (e.g., maximum inter-story drift ratio) imposed on modern, ductile RC moment frame buildings with different dynamic properties, particularly at locations impacted by strong forward directivity effects; (2) to develop new insight into the relationships between geophysical parameters (fault rupture characteristics and geological structure) and the structural response of RC buildings; (3) to examine the ability of physics-based deterministic simulations to represent the characteristics of recorded ground motions, and to provide insight for improving future simulation approaches.

The following section describes the characteristics of the archetype RC buildings designed for this study, in addition to the properties of the numerical structural models, ground motion simulations, and underlying fault rupture scenarios. The remainder of the article reports important findings on the regional-scale spatial variability of structural risk, the significance and spatial extent of forward directivity effects on buildings with different frequency content, and the impact of fault rupture characteristics and site conditions on the induced structural demands near the fault.

2 | PROPERTIES OF THE SIMULATION MODELS

2.1 | Description of the building designs and structural simulations

Two archetype RC buildings were designed for seismic category E: a 3-story building and a 12-story building. The building frames were designed as special moment-resisting frames following the seismic provisions of ASCE 7-16[7] and the RC provisions in ACI 318-14.[28] The seismic design is based on the risk-targeted maps for a site that is about 2 km away from the Hayward fault in Berkeley, California with site class C, which was selected based on the shear wave velocity profile in the computational domain, where the average shear wave velocity in the top 30 m (V_{s-30}) ranges between 380 m/s for basin soils to 500 m/s for rock. The maximum considered earthquake spectral response acceleration parameters at short periods and at a period of 1 s, respectively, are $S_s = 2.154$ and $S_1 = 0.83$. These accelerations are representative of a high-hazard, near-fault seismic region. The buildings were designed to resist the seismic forces using all interior and exterior frames in each orthogonal direction, and both were designed using normal-strength concrete and steel materials. The geometry, seismic response coefficient, and computed first-mode period for each building are listed in Table 1.

Two-dimensional (2D) structural simulation models of representative building frames were created using the structural analysis platform Opensees.[29] The structural components are simulated using the lumped plasticity (or nonlinear hinge) modeling approach,[30] in which the inelastic behavior of the structural member is assumed to be concentrated at the member ends only. Springs at both ends of each member cumulatively simulate the nonlinear effects due to strength and stiffness degradation of concrete and steel, steel rebar buckling and fracture, and bond slip between steel rebar and the surrounding concrete. The modified Ibarra–Medina–Krawinkler (IMK)[31] material model with peak-oriented hysteretic response is used to represent the constitutive behavior of the nonlinear springs, which is idealized as a multilinear moment-rotation relationship. The IMK model parameters characterize the yield, plastic and post-capping hinge rotation

capacities, the initial, post-yield, and post-capping stiffness, and cyclic deterioration parameters, which determine the energy dissipated during each loading cycle. The values of the IMK model parameters were computed using the prediction equations developed by Haselton et al.,[32] which are based on statistical regression analysis of RC columns failing in flexure and combined shear-flexural modes (brittle shear failures are not considered). The lumped plasticity modeling approach was selected for this study because of its computational efficiency, as compared to other modeling approaches, and its ability to simulate the nonlinear dynamic response of RC buildings from damage initiation to the onset of sidesway collapse. Geometric nonlinearity effects are incorporated using a corotational geometric transformation, and all models are assumed to have a fixed-base boundary condition; therefore, soil flexibility and potential soil–structure interaction effects are disregarded. Rayleigh damping corresponding to 5% of the critical damping ratio is applied in the first and third modes of vibration. The simulation models are subjected to earthquake ground motion acceleration time series in a nonlinear time history analysis framework with a Newmark integration scheme, and the building response quantities are recorded at each time step of the analysis. The structural analyses were conducted in a set of parallel simulations using the CORI computer at the National Energy Research Scientific Computing Center at Lawrence Berkeley National Laboratory.

2.2 | Description of the earthquake ground motions

The ground motion acceleration time series were generated using the finite difference code SW4 (Seismic Waves, fourth order) developed at Lawrence Livermore National Laboratory,[33] which simulates seismic waves using 3D earth models on distributed-memory parallel computers, and includes anelastic attenuation and mesh refinement capabilities. The simulations can capture important site and path effects, such as focusing and scattering of seismic waves and motion amplification by sedimentary basins. The kinematic earthquake rupture modeling technique of Graves and Pitarka is used to simulate the fault rupture processes[25,34]; this technique has been validated in simulations of recorded earthquakes.[34,35] Given the large computational requirement in deterministic 3D wave propagation modeling, our maximum modeled frequency is 5 Hz. Doubling the modeled frequency range for the same minimum shear wave velocity increases the computational demand by a factor of 16. We do not include stochastic variability in our velocity model. The effects of 3D small-scale velocity variations on the simulated ground motion and building response will be the subject of future studies. A magnitude 7.0 strike-slip earthquake was simulated with a fault length of 62.6 km and fault width of 16 km. The rupture velocity is set to 80% of the local shear wave velocity, which is consistent with observed rupture velocity values found for shallow crustal earthquakes. The depth below the ground surface to the top of the fault was set to 0.2 km and the dip angle is 90 degrees. Three different rupture scenarios (A, B, and C) were generated using the rupture models shown in Figure 1. These models are representative of the fault rupture in common shallow crustal earthquakes with a predominantly strike-slip mechanism. The three selected scenarios have different slip distribution characteristics (asperities) and are capable of producing directivity effects with varying strength. Scenario A utilizes a fully stochastic distribution of slip (and is referred to as the stochastic rupture scenario), and scenarios B and C contain distinct patches of large slip (250–500 cm) at different locations along the fault (Figures 1B and 1C) and are referred to as the hybrid rupture scenarios (not to be confused with the hybrid simulation approach of ground motions). Based on observations from previous earthquakes, near-fault ground motions can be significantly influenced by the slip distribution on the fault. Ruptures with localized areas of shallow large slip can result in large ground motion amplitudes at sites near these slip patches (e.g., the 2016 Kumamoto, Japan earthquake).[34] This very localized ground motion amplification can result in a significant increase in the structural demands. The inclusion of rupture scenarios with distinct large-slip patches is thus an important consideration in structural demand simulations. Further details about the rupture model can be found in Graves and Pitarka,[25] and validations of the generated ground motions are available in Pitarka et al.[34] and Rodgers et al.[26]

The computational domain spans 100 km × 40 km × 30 km, with a minimum grid spacing of 8 m, and incorporates 3D geological features and a flat earth surface. The area north of the fault contains a shallow sedimentary basin (600 m deep with an approximately 90-degree basin-edge dip angle) and that south of the fault is rock, as shown in Figure 2(A) and (B). These conditions allow for studying the amplification effects in the near-fault area due to the basin. The location of the epicenter is marked with a star in the same plot. The surface of the domain contains 3861 stations—spaced at 1 km intervals—at which three ground acceleration history components are generated: a horizontal fault-normal (FN) component, a horizontal fault-parallel (FP) component, and a vertical component. Each 2D building model is assumed to be replicated at all 3861 stations, and is subjected to the FN and FP horizontal components separately. A total of 46,332 nonlinear building response history simulations were conducted, and representative results from all simulations are discussed in the following sections.

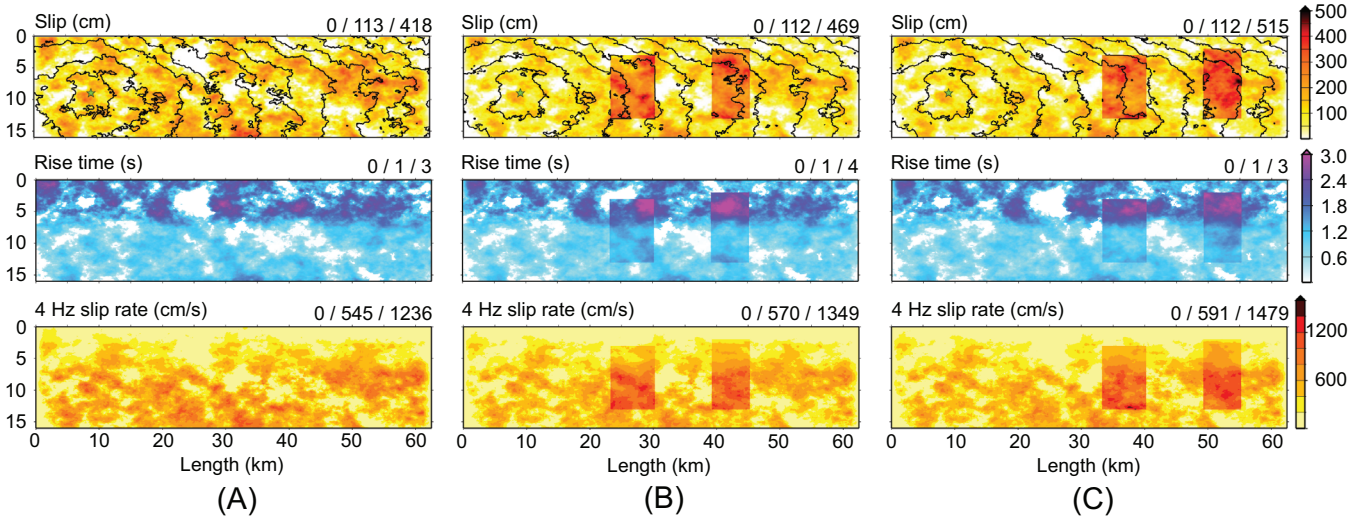

FIGURE 1 Rupture models used in ground motion simulations of M7 scenario earthquakes on a vertical strike-slip fault. The first row shows the slip distributions, the second row shows the rise time, and third row shows the peak slip rate computed after low-pass filtering the source time function at 4 Hz. The triplet of numbers at the upper right of each panel indicates the minimum, average, and maximum values of the parameter being displayed. Isochrones plotted on the slip distribution indicate rupture front at 2 s time intervals: (A) rupture scenario A; (B) rupture scenario B; (C) rupture scenario C

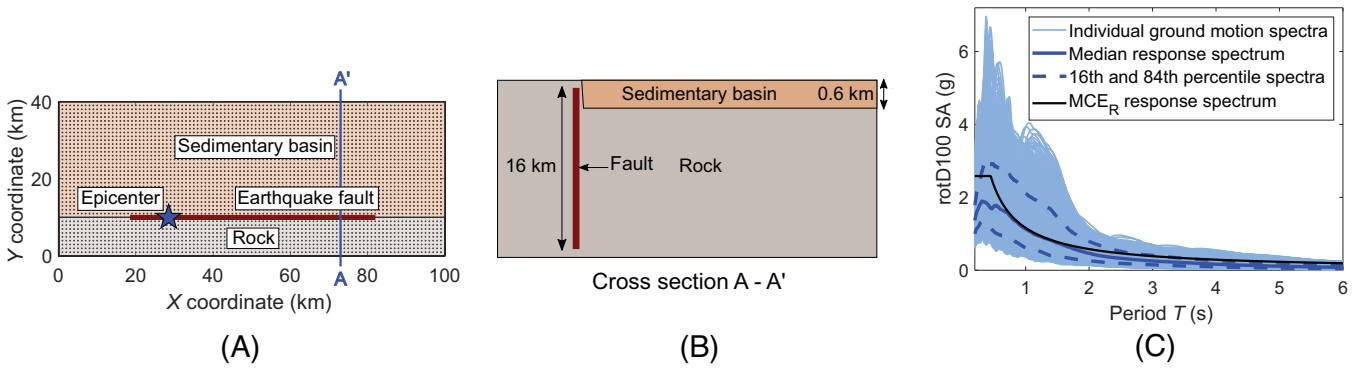

FIGURE 2 (A) Plane view of the computational domain showing the fault trace, epicenter, surface stations, and relevant geologic features; (B) cross-sectional view showing the basin and rock soils; (C) maximum-direction acceleration spectra for the simulated motions within 2 km of the fault and the maximum considered earthquake spectrum for the selected building site

In most of the following text, only the relative differences in the predicted structural demands are of interest. However, preliminary interpretation of the structural risk to the archetype buildings in an absolute sense necessitates an understanding of the relative intensity of the simulated ground motions compared to the risk-targeted maximum considered earthquake (MCE_R) design spectrum for the buildings created in this study. Such a comparison is shown in Figure 2(C) for the maximum-direction acceleration response spectra of the simulated motions within a 2-km closest distance to the fault. The comparison demonstrates that the simulated scenarios generate higher intensity ground motions within a 2-km distance at most periods than the MCE_R spectrum. Between 0.5 and 2 s in particular, the 84th percentile spectrum of the simulated motions is significantly higher than the MCE_R spectrum, which represents a bounded minimum of the probabilistic and 84th percentile deterministic MCE ground motion intensities at the selected site. This observation implies that the structural risk, particularly to the 3-story building, due to the simulated near-fault ground motions may be higher than the risk associated with the MCE_R spectrum at the selected building location. It is important to emphasize that the same building design is replicated everywhere in the domain; therefore, the design characteristics at each unique distance from the fault do not represent the expected code standards at that location. The uniformity of the building design over the domain allows for studying the relative differences in the structural demands due to the source, path, and site effects.

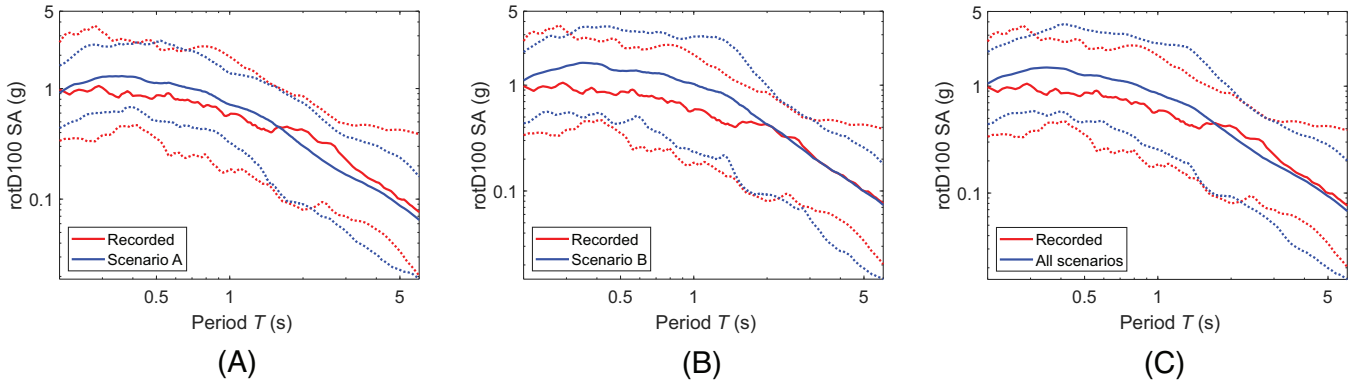

FIGURE 3 Maximum-direction orientation-independent median, and 2.5 and 97.5 percentile acceleration response spectra of near-fault real (recorded) ground motions along with the simulated motions of: (A) scenario A; (B) scenario B; (C) all scenarios

3 | CHARACTERISTICS OF THE SIMULATED AND RECORDED GROUND MOTIONS

Examining the characteristics of the simulated ground motions and the associated structural demands against the characteristics of real records is an important step toward establishing the use of earthquake simulations in engineering risk assessments. Comparisons of the intensity of the simulated motions against available records in the near-fault region were performed using a subset of shallow crustal earthquake records compiled by Baker et al.,[36] which include ground motions with relatively strong velocity pulses within approximately a 10-km closest distance to the fault. The dataset consists of 38 records from seven different earthquakes with moment magnitudes ranging between 6.53 and 7.62, with an average of 7.11, and spans a wide range of V_{s-30} with an average value 404 m/s. This dataset was compared against the 4728 simulated ground motions within a 10-km closest distance generated by M7.0 pure strike-slip ruptures, with an average V_{s-30} of 436 m/s. Because the FN and FP acceleration components of the real records were readily available, direct comparison against the corresponding components of the generated ground motions was possible. This equivalence is particularly important at short distances because near-fault motions are known to be polarized, such that the FN component intensity is usually much higher than the FP component. The comparison against the available real records, however, has several limitations: (1) the records may not sufficiently represent the full extent of the expected variability at short distances; (2) the recorded motions are from earthquakes in different regions, with varying magnitudes and site conditions, whereas the simulated ground motions share the same magnitude and site conditions; (3) the recorded dataset corresponds to a variety of rupture mechanisms and may be associated with certain approximations in estimating the fault orientation; and (4) several rupture characteristics such as the depth to the top-of-rupture and the dip angle are not considered in the comparison and may lead to significant differences between the simulated and recorded data. Nonetheless, the comparison serves to assess the ability of the simulations to reasonably represent the characteristics of real ground motions over a broad range of frequencies, contextualizes the findings of this study with respect to structural risk estimates, and provides important insight to support the development of new rupture simulations.

Figure 3 shows an orientation-independent measure of the maximum-direction spectral acceleration—or rotD100[37]—of the simulated motions within a 10-km closest distance overlaid on top of the spectra of real records. The median and 2.5 and 97.5 percentile spectra of the records of scenario A (Figure 3(A)) agree reasonably well with those of the recorded dataset over a broad frequency band. The simulated ground motions, however, have consistently higher median spectral accelerations in the short-period range (up to a period of about 1.7 s) than the real motions. Scenario A motions also have lower median spectral accelerations in the mid- to long-period range, meaning that this scenario would potentially underestimate the seismic hazard and risk for long-period structures. Scenarios B and C generally have higher spectral accelerations over most periods than scenario A. This feature improves the agreement between the spectra of the simulated and real ground motions in the long-period range, as seen in Figure 3(B) for scenario B, and supports the use of the hybrid rupture scenarios to assess the risk to long-period structures. The median and 2.5 and 97.5 percentile spectra of all three scenarios in Figure 3(C) exhibit better agreement with the available dataset, particularly in the long-period range.

The attenuation trends of common ground motion intensity measures (the spectral acceleration at the first-mode period of both buildings $SA(T_1)$ and the peak ground velocity (PGV)), as the distance from the fault increases, support the preceding observations. Representative plots in Figure 4 display the median and 2.5 and 97.5 percentile intensities of the FN

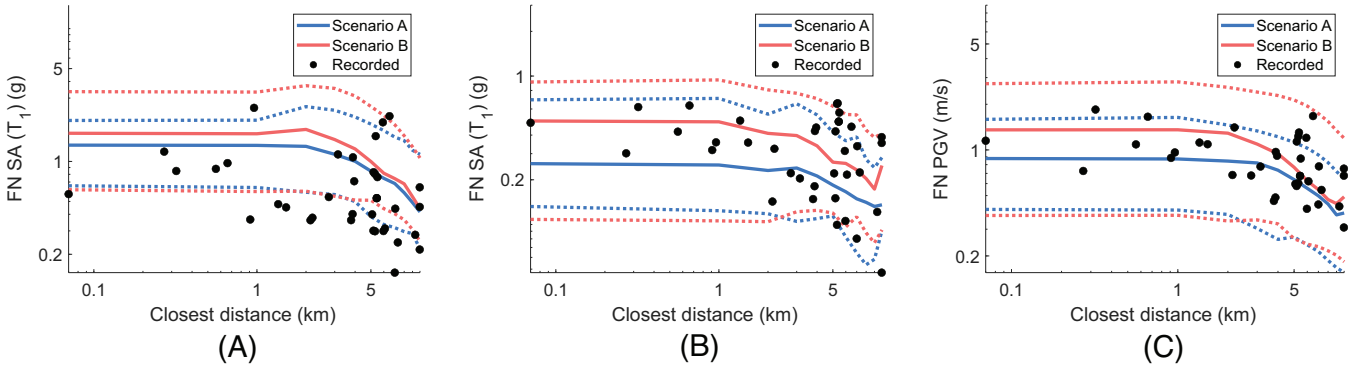

FIGURE 4 Median and 2.5 and 97.5 percentile values of the intensity measures of the simulated ground motions in scenarios A and B versus the closest distance to the fault: (A) $SA(T_1)$ for the 3-story building; (B) $SA(T_1)$ for the 12-story building; (C) peak ground velocity. The corresponding data points of the available real ground motions at distances less than 10 km are also plotted

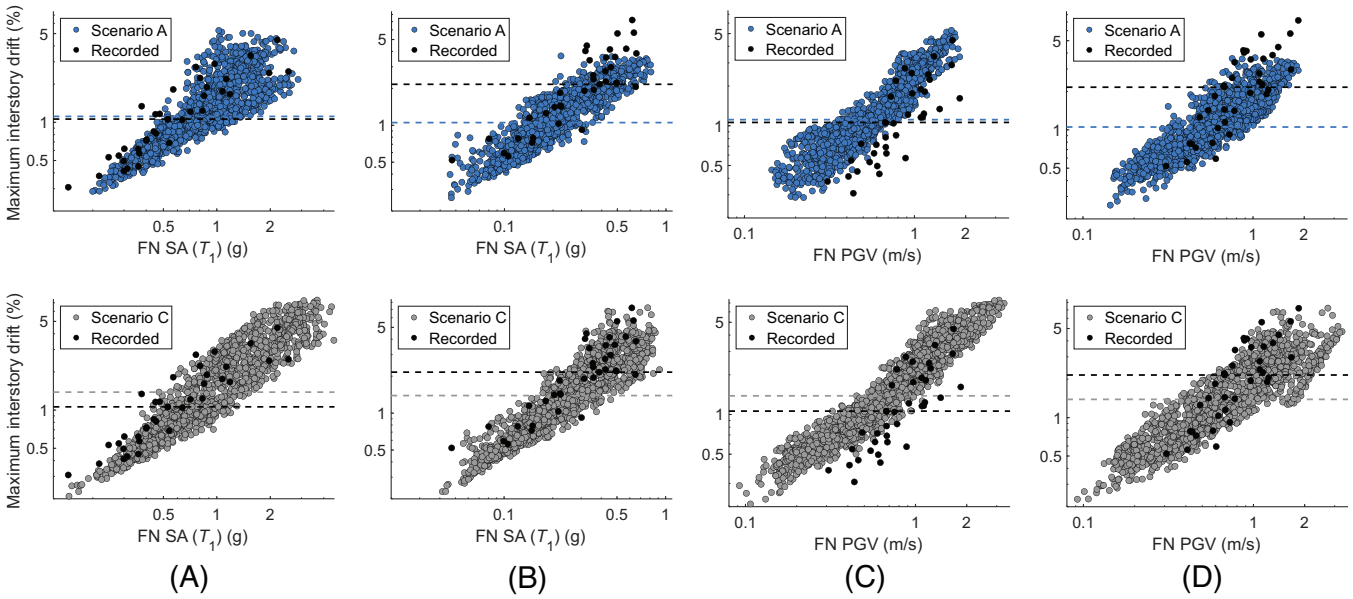

FIGURE 5 MIDR demands of the recorded and simulated ground motions (scenarios A and C) plotted against: (A) $SA(T_1)$ for the 3-story building; (B) $SA(T_1)$ for the 12-story building; (C) PGV for the 3-story building; (D) PGV for the 12-story building

component of scenarios A and B within a 10-km distance along the length of the rupturing fault (1280 synthetic records for each scenario). The corresponding intensities of the real recorded motions within 10 km and their closest fault distance are also plotted. In general, the 95% interval of all the intensity measures at distances between 1 and 10 km exhibits consistency with the real recordings, although the plots emphasize that the presence of the slip patches in scenario B substantially increases the median and 97.5 percentile spectral accelerations and peak ground velocities compared to scenario A. For distances shorter than 1 km, very few real records are available and the results of the simulations are yet to be assessed against near-fault recordings as they become available. Based on the comparisons in subplots B and C, the presence of the slip patches in scenario B better reflects the range of the recorded low-frequency spectral accelerations ($SA(2.23s)$) and the PGV particularly between 5 and 10 km closest distance, as compared to scenario A which does not incorporate slip patches. Subplot A represents the high-frequency spectral acceleration ($SA(0.75s)$) and shows several real SA values between 1 and 10 km that are lower than the 2.5 percentile SA in all the simulated scenarios. It is worth noting that 16 of the plotted 37 real motions in Figure 4 belong to the Chi-Chi Taiwan earthquake, which has been previously documented to contain unusually low short-period spectral accelerations in the near field.[38]

Figure 5 displays the maximum structural demands, in terms of the maximum interstory drift ratio (MIDR), on the 3-story and 12-story buildings plotted against $SA(T_1)$ and the PGV of the FN component of simulated (scenarios A and

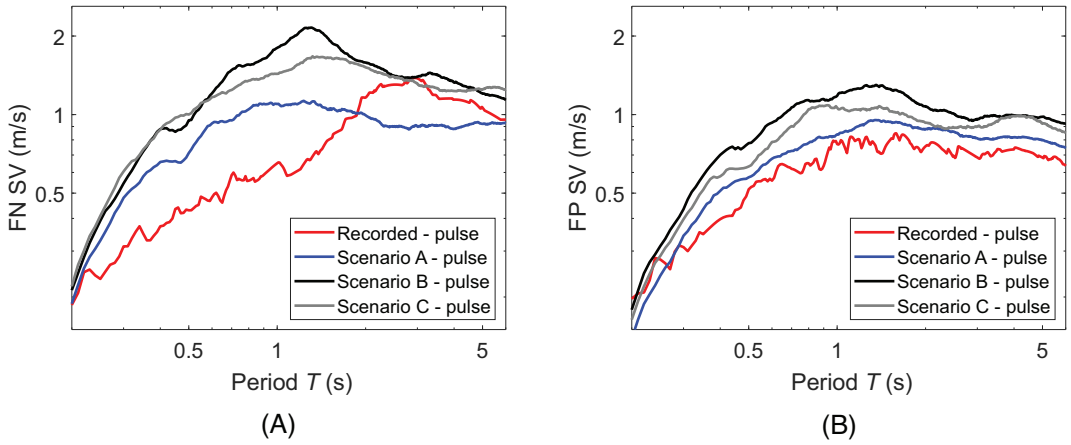

FIGURE 6 Median velocity response spectra for pulse-type ground motions: (A) FN component; (B) FP component

C) and recorded ground motions approximately within a 10-km closest distance. The median demands of each dataset are also marked in each subplot. The highly dense simulated datasets highlight the large dispersion in the correlation between the spectral accelerations and the MIDR for both buildings in the near-fault region (subplots A and B), particularly at very short distances (large SA values). The trends of the structural demands induced by all scenarios in both structures are generally consistent with those induced by the real recorded motions. The median MIDR demand on the 3-story building due to scenario A is almost identical to that due to the recorded dataset. However, the hybrid rupture scenario C, which is associated with higher short-period spectral content, imposes more significant structural demands on the 3-story building as compared to the demands induced by the recorded motions. The opposite trend is evident in the response of the 12-story building, such that the MIDR median due to the recorded motions is higher than the medians of all ground motion simulations, which may suggest potential deficiencies of the simulations in the long-period range. As expected, the demands imposed on the 12-story building by scenarios B and C are closer to those of the recorded motions (with a 27% differences), whereas the median demand of scenario A is about 50% less than that of the available real records.

The correlation between the PGV and structural demands (subplots C and D) also demonstrates important differences between the frequency content of the simulated and recorded motions. In particular, many real records impose lower structural demands on the short-period building than the simulated motions with similar PGV values. Our analysis reveals that the velocity pulses of the recorded motions, on average, have lower frequency content than the simulated motions (particularly those from the hybrid rupture scenarios). To examine the pulse characteristics of the simulated motions, an automated and objective algorithm[39] was employed to classify the ground motions as pulse or nonpulse, depending on the presence of strong pulses in the velocity time histories. The pulse frequency content of each ground motion set is assessed via the mean period of the velocity pulses of the pulse-type records. The mean pulse period for all simulated scenarios (and considering pulses detected in all orientations) is 2.9 s, whereas that of the recorded motions is 5.7 s. This difference indicates that the recorded motions have significantly longer period energy than the simulated motions, and is visually apparent in the median velocity spectra of the FN components in Figure 6(A), in which the distinctive "peaks" are expected to reflect the pulse frequency content of each dataset. All simulated scenarios have higher spectral energy in the short- to mid-period range (up to a period of about 2 s) than the recorded dataset, and scenarios B and C have significantly higher energy than scenario A. In addition, the spectra for scenarios B and C contain a distinctive peak near a period of 1.5 s, whereas the spectrum of the recorded motions peaks at a much longer period of about 3 s. Scenario A, on the other hand, has a similar energy content to the recorded motions, although it does not possess a prominent peak, which suggests the presence of pulses with a broad range of frequencies. The substantial differences between the ground motion sets are only seen in the FN component, whereas the FP components are found to be rather similar (Figure 6(B)). Several factors are likely behind the differences in the pulse frequency content between the simulated and recorded motions; most notably, the geometry and distribution of the rupture asperities along the fault. Because these differences decrease significantly at longer periods, the response of the 12-story building to the simulated ground motions agrees with its response to the recorded dataset (Figure 5(D)), despite the presence of significant ground velocities in the hybrid rupture scenarios (upwards of 200 cm/s). The comparison against the available records suggests that the hybrid rupture scenarios with localized slip

regions may offer appropriate risk estimates for long-period structures, and somewhat conservative estimates for short-period structures. It is worth noting that the impact of pulse-type motions on the structural demands strongly depends on the relationship between the effective structural period and the frequency content of the largest velocity pulse[40]; this topic is, however, beyond the scope of this article.

4 | REGIONAL-SCALE SPATIAL VARIABILITY OF RISK TO MODERN RC BUILDINGS

The variability of structural risk within a given earthquake scenario (spatial variability) and between different rupture scenarios (sometimes referred to as temporal variability) is the primary focus of this study. Important aspects of the response of RC buildings to the simulated ground motions are characterized with respect to (1) the differences in the structural demand trends between near-fault and far-field locations, and along the rupturing fault in the forward directivity region; (2) the effects of introducing large-scale high slip patches to the rupture model on the structural demands; and (3) the effects of site conditions on the structural demands near the fault. The structural response quantities of interest are

- *The maximum interstory drift ratio*: This parameter is ubiquitously used to judge the structural member deformation demands and define damage limit states for buildings, and is expected to provide a reasonable estimate of the structure's ability to resist sidesway collapse. MIDR limits of 0.5%, 1.0%, 1.5%, and 2.5% are used per ASCE 43-05[41] to refer to expected damage states in RC buildings. These limits are surmised to correspond to essentially elastic behavior, limited plasticity, moderate plasticity, and large plasticity, respectively. Despite the dependence of the damage states on the building ductility, the MIDR provides valuable insight on the relative expected deformation demands.
- *The largest rotation experienced in the plastic hinges at the end of a structural member (beam or column)*: This measure relates more directly to the plastic rotation capacity of the structural member and is capable of predicting a localized loss in the load-carrying capacity after a plastic hinge reaches its rotation capacity. This measure is presented as a demand-to-capacity ratio; that is, a ratio of the maximum rotation demand experienced in a member to its plastic capacity. Although it depends on the assumptions and calibrations associated with the lumped-plasticity modeling approach, this measure is useful in a relative sense to judge the variability of component demands.

4.1 | Spatial variability of structural demands

The map plots in Figure 7 represent the MIDR demands on the 12-story building due to the three rupture scenarios. The maps demonstrate that the FN component of each scenario exhibits a strong directivity effect that is concentrated within about 10 km of the fault and characterized by significant structural demands. The FP component, on the other hand, imposes relatively low demands that are more pervasive over the entire domain, particularly in the hybrid rupture scenarios. For both buildings, the FN MIDR demands over most of the domain do not exceed 3.5%. However, in a small number of locations at very short distances from the fault (up to about 5 km) in the forward directivity zone, MIDR up to 7% is observed; these large demands are particularly seen in scenarios B and C, which are more damaging than scenario A. Although most of the structural demands are within the expected ductility capacity of RC special moment frames, a small number of buildings within 1 km of the fault contain structural members which marginally exceed their plastic rotation capacity and/or form plastic hinges in the columns (which suggests a possible story mechanism); these buildings are judged to be near collapse based on the plastic hinge formation, but the numerical model does not specifically indicate unbounded drift growth as a numerical manifestation of collapse. Since the primary demand parameter of interest to this study is the MIDR and its variability across the domain, these buildings are handled in the same way as the rest of the buildings over the domain.

The near-fault region is also associated with significant variability in the structural demands. For example, at a 1-km distance, the 3-story MIDR varies by a factor up to 7.9 along the length of the fault (this factor is defined as the ratio of the maximum to minimum MIDR at the designated distance). The large variability near the forward directivity zone can be demonstrated by examining the statistical distributions of the structural demands along the length of the fault at different normal distances. Examples of such plots are shown for scenario C in Figure 8, which highlights the expected values and dispersion associated with the MIDR at 1, 10, and 15 km due to the variability of the ground shaking. These distributions describe the probabilities of not exceeding discrete MIDR values, and a cumulative lognormal distribution is fitted to each dataset to estimate the dispersion. For the FN component of motions, the dispersion in the MIDR is highest

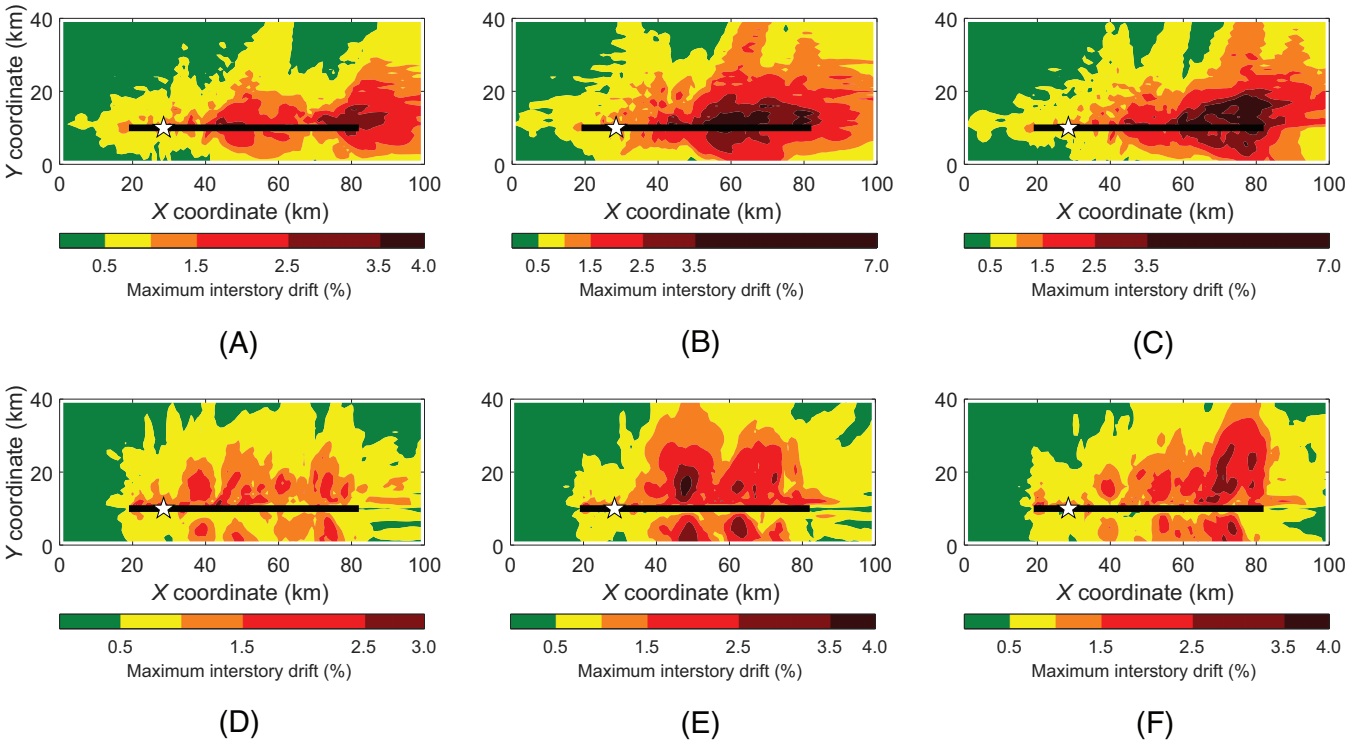

FIGURE 7 Map representation of the MIDR demands on the 12-story building due to (A) the FN component of scenario A; (B) the FN component of scenario B; (C) the FN component of scenario C; (D) the FP component of scenario A; (E) the FP component of scenario B; (F) the FP component of scenario C

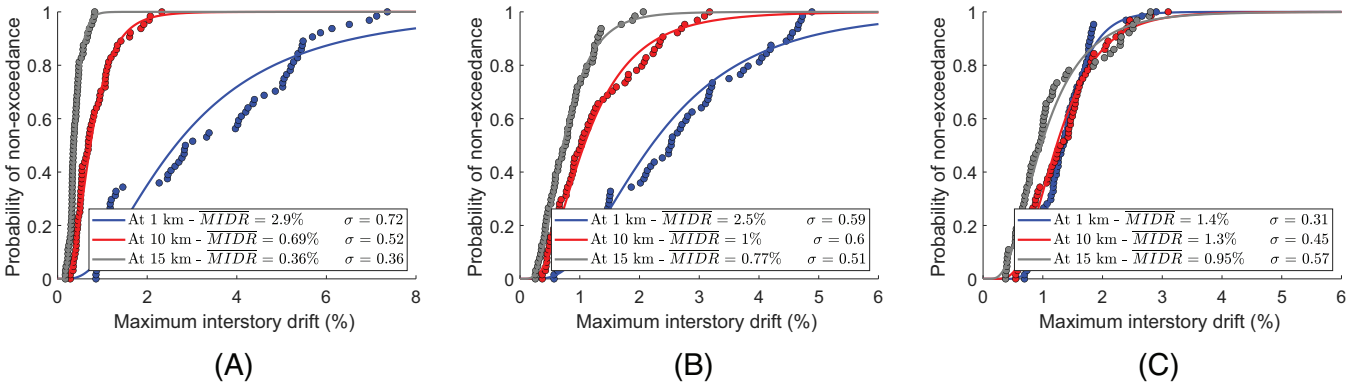

FIGURE 8 MIDR distributions for rupture scenario C along the fault length at several distances due to (A) the FN component on the 3-story building; (B) the FN component on the 12-story building; (C) the FP component on the 12-story building

at 1 km for both buildings and all scenarios. At a 10-km distance from the fault, the median ground motion intensity and structural demands decrease significantly, but the dispersion remains relatively high, particularly for the flexible building. For example, the median MIDR demands for the 3-story and 12-story buildings decrease by factors of 4.4 and 2.3, respectively, between the data points at a 1-km and 10-km, whereas the average dispersion (in terms of logarithmic standard deviation) over all scenarios remains almost the same for both buildings. Although the variability of the FN component demands drops beyond 15 km, the FP component demands are found to have a significant dispersion at longer distances from the fault, particularly in the scenarios with high-slip regions. The distributions in Figure 8(C) demonstrate that, although the FP component demands are substantially lower than those induced by the FN component, the logarithmic standard deviation increases by 84% between the FP demands at 1 km and 15 km distance. This observation points to

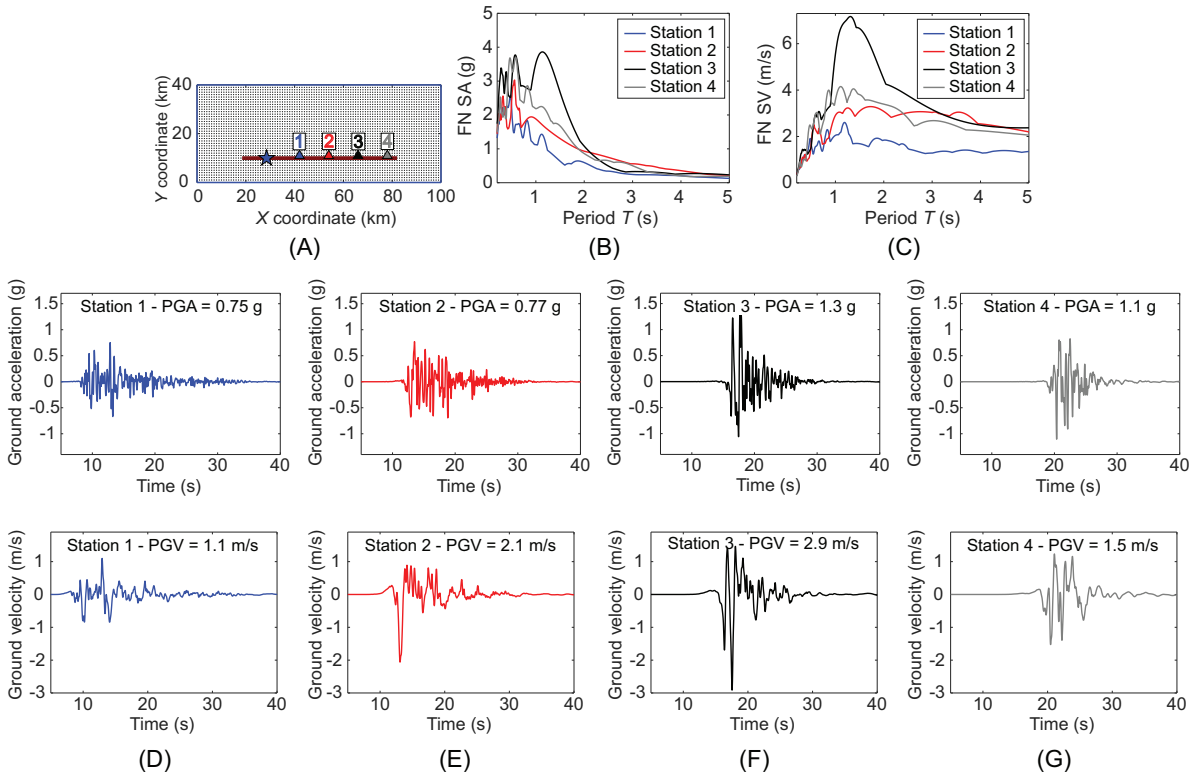

FIGURE 9 FN ground motion properties at stations 1–4 in rupture scenario B: (A) locations of the stations; (B) acceleration response spectra; (C) velocity response spectra; (D) acceleration and velocity histories at station 1; (E) acceleration and velocity histories at station 2; (F) acceleration and velocity histories at station 3; (G) acceleration and velocity histories at station 4

important effects that may be present in the FP component of ground motions, particularly those recorded near high-slip regions.

The deformation demands on the 3-story building near the fault are found to be higher than those imposed on the 12-story building, which is attributed to the frequency content of the ground motions. In contrast, the demands on the 12-story building exhibit wider dispersion at locations beyond 10 km; a trend that is likely caused by the slower attenuation of the low-frequency waves. The substantial variability of the structural response quantities found at short distances, and seen to persist at longer distances for the flexible building, has profound implications on seismic risk assessment. The findings of this study indicate that identical buildings at identical short distances may experience radically different structural demands. These findings strongly support performance-based design, which is driven by the ground motion variability (among other sources of uncertainty), as an appropriate approach for characterizing the risk at near-fault sites. Such an approach is only feasible when enough recorded or rigorously simulated ground motions are available to represent the statistical dispersion expected near the fault.

Within the region expected to experience strong rupture directivity effects, the FN structural demands are shown to increase with increasing distance from the rupture initiation (measured parallel to the fault) up to a certain distance that depends on the details of the rupture scenario. For all scenarios in this study, the peak structural demands induced by the FN component are located between 29 and 55 km away from the rupture source (along the fault). Beyond 55 km, the structural demands drop significantly and are close to the demands in the backward directivity region (behind the rupture initiation). The rupture directivity effects are analyzed at four stations in scenario B: stations 1–4 shown in Figure 9(A). This group of stations is located 1 km normal to the fault and 13.5, 25.5, 37.5, and 49.5 km away from the rupture initiation, respectively. Figures 9(D)–9(G) show the acceleration and velocity time series of the FN component at each station, whereas Figures 9(B) and 9(C) show plots of the spectral acceleration and velocity for the same records. The plots demonstrate the expected effect of accumulating the seismic waves as the rupture propagates toward each station, particularly in the velocity time histories. Although the peak ground acceleration (PGA) increases by only 3% between stations 1 and 2, the PGV increases by 91% and the peak ground displacement (not shown) increases by 153%. Despite the fact that all four stations lie in the forward directivity path, stations 2 and 3 experience the strongest ground acceleration, velocity, and

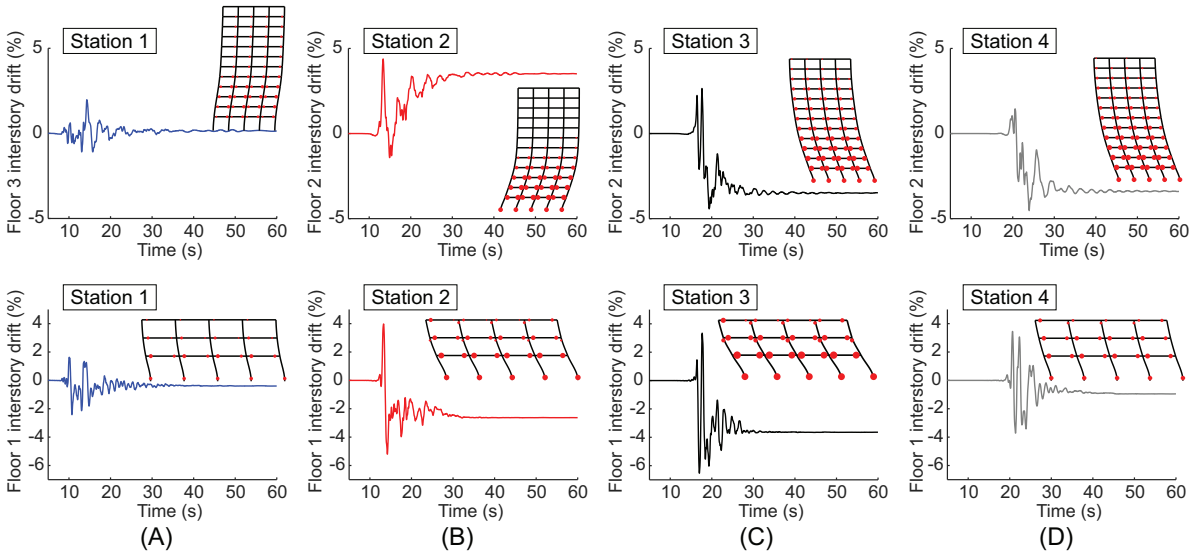

FIGURE 10 Deformed shape, plastic hinge locations, and maximum floor drift histories for the 12-story and 3-story buildings due to scenario B at (A) station 1; (B) station 2; (C) station 3; (D) station 4. Building deformations are shown at the time instance where the structure experiences the largest MIDR over the entire time history

displacement pulses. The peak velocities (and peak structural demands) are experienced near station 3, which is about 37.5 km away from the source. At station 4, the peak ground velocity and displacement amplitudes decline by 48% and 36%, respectively, whereas the acceleration amplitudes do not substantially change. The spectral demands are also seen to increase significantly between stations 1 and 3, particularly for periods between 1 and 2 s, then drop at station 4.

An idealization of the corresponding building deformations is shown in Figure 10, in addition to the interstory drift time histories of the floor experiencing the maximum drift at each station. The deformed shape plots include a visual measure of the plasticity experienced by the structural components, which is represented by the plastic rotation of the nonlinear springs at each beam and column end, and plotted as red circles whose size scales up with the value of the plastic rotation. The plastic hinges qualitatively identify the largest rotation demands in the structure, and flag members where the plastic hinge rotation capacity has been exceeded, which signifies the start of softening (loss of load carrying capacity) due to nonlinear effects. The plots indicate that station 1, although closest to the rupture initiation, experiences less than half the demands at stations that are further along the fault. The 3-story building experiences the highest demands at stations 2 and 3, up to 6.6% MIDR and a maximum rotation demand close to 100% of the rotation capacity at station 3 (i.e., at least one plastic hinge reaches its full plastic rotation capacity, which can be viewed as an indicator of significant damage in the structural components). The 12-story building exhibits a severe response at stations 2–4, and varying demand distributions along its height, which indicates sensitivity to various frequency components. The drift history plots also show relatively large residual drifts associated with the buildings at stations 2–4. Further analysis reveals that significant permanent drifts are common in buildings located in the forward directivity region at short distances and diminish beyond 10 km away from the fault. Similar to the maximum demands, the residual drifts were found to depend on the frequency characteristics of the building. For example, the 3-story building experiences the largest residual interstory drifts at station 3 (about 3.6%), whereas the 12-story building experiences large permanent drifts at stations 2–4 (between 3.4% and 3.5%). Because residual drifts typically correlate with building repairability, identifying near-fault regions associated with large residual demands may be important for engineering risk assessments at near-fault sites.

4.2 | Effect of the fault slip characteristics on structural response

Studies of large earthquakes have shown that hybrid rupture models which combine large-slip features with stochastic small-scale variations are better able to reproduce the characteristics of observed earthquakes over a broad range of frequencies.[34,42] However, the effect of including these high-slip regions in the rupture models on structural risk and reliability assessments is not fully understood. This study indicates that localized slip regions can substantially increase

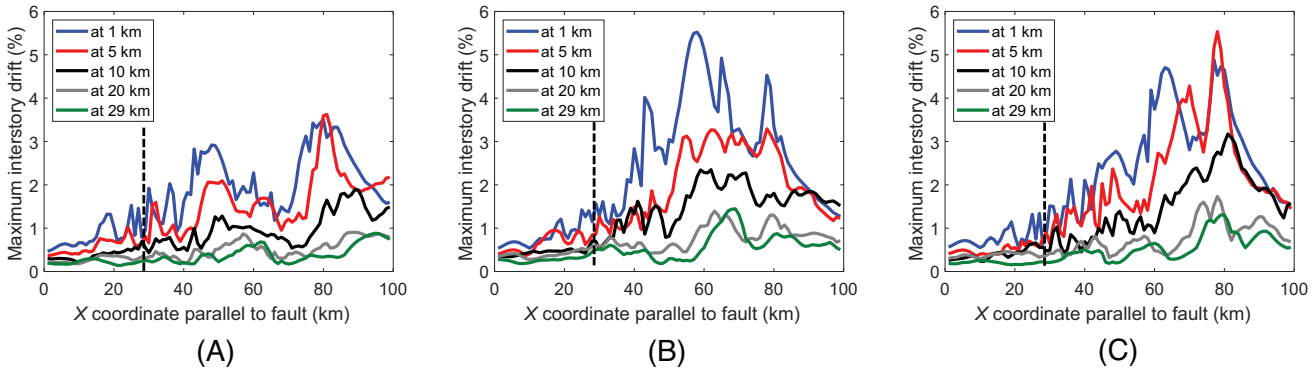

FIGURE 11 Trends of the MIDR demands on the 12-story building parallel to the fault due to the FN component of the ground motions of: (a) scenario A; (b) scenario B; (c) scenario C

the demands imposed on structures located near the fault. These effects are apparent in the risk map plots of Figure 7, and further highlighted in the line plots of Figure 11 which represent the 12-story MIDR along several normal distances from the fault. The presence of the slip patches is shown to impact both the magnitude and the relative locations of the highest ground motion intensity and structural response quantities, such that stations proximate to the patches experience the highest demands. For example, the largest MIDRs in scenario B are near $x = 65$ km, whereas the maxima in scenario C are near $x = 80$ km; both points are close to the locations of the slip patches in each scenario (see Figure 1). Despite having no deterministic patches, the demands in scenario A exhibit multiple peaks because the stochastic nature of the slip yields some slip concentrations. However, these concentrations typically have lower slip rates than the patches in the hybrid rupture scenarios. Therefore, the demands of scenarios B and C over regions of the domain that are forward of the slip patches (in the direction of rupture) are significantly higher than those of scenario A. Similar trends are observed for the spectral accelerations and peak ground velocities.

The geographically varying effects of the rupture asperities on near-fault sites are highlighted by examining the response spectra and waveforms of ground motions at stations that are proximate to and in the forward direction of the asperities. The locations of three of these stations relative to the localized slip patches are plotted in Figures 12(A) and 12(B), for scenarios B and C, respectively, and the remaining subplots show the response spectra at the three stations. In addition, the ground acceleration and velocity time histories at station 3 are plotted in Figure 13. Examining the response spectra in Figure 12 reveals that the effects of the concentrated slip in the forward directivity zone are largest at stations immediately following the slip patches and decrease as the distance from the asperities increases. The localized slip in scenario B primarily impacts the mid- to long-period component, whereas the slip patches in scenario C have higher impact on the short-period component. For example, the scenario B PGV at station 2 is amplified by 62% compared to scenario A, yet the peak ground accelerations are lower than scenario A by 18%. Similarly, at station 3, the ratios of the PGA and PGV of scenario B/scenario A are 1.2 and 2.6, indicating a primarily low-frequency effect. On the other hand, the ratios of the PGA and PGV of scenario C/scenario A are 1.5 and 1.6, respectively, indicating both low- and high-frequency component amplification. At station 4—which is close to the end of the scenario C asperities—a similar broadband impact on the ground motion intensity is observed in Scenario C, such that both the peak acceleration and velocity are amplified by factors of 2.8 and 2.4, compared to scenario A. A modest impact is seen at station 4 in scenario B because this station is relatively far from the slip patches. These differences suggest that the placement of the high-slip patches in the rupture model may have a moderate impact on the frequency range of the amplified ground motion intensity relative to stochastic rupture scenarios.

To examine the impact of the high-slip regions on the median structural demands and associated dispersion, distributions of the MIDRs along the length of the fault at several distances were plotted for all scenarios. Examples of such plots are shown in Figure 14, along with the median values and the logarithmic standard deviation of the fitted lognormal distributions. Analysis of these plots reveals that the median demands associated with the scenarios B and C are consistently higher than those associated with scenario A at all distances. For example, the average median MIDR due to the FN component of scenarios B and C for the 12-story building is 1.5 and 1.7 times that of scenario A at a distance of 1 and 15 km, respectively. The FP component demands are impacted more substantially by the presence of the patches at distances between 10 and 20 km from the fault than at shorter distances. For instance, at a 20-km distance, the FP MIDR

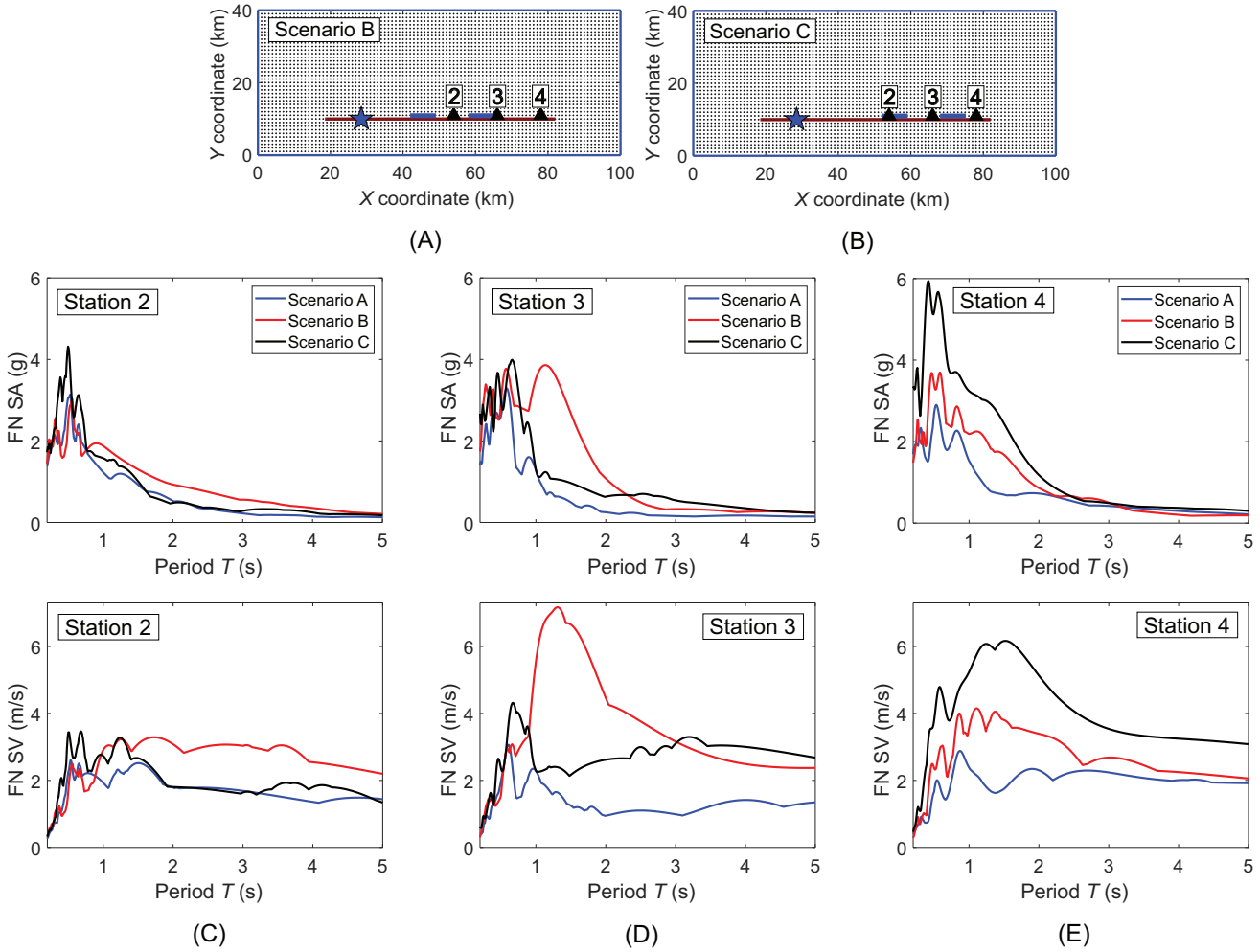

FIGURE 12 Response spectra at stations 2–4 for all three rupture scenarios: (A) locations of the stations relative to the slip patches of scenario B; (B) locations of the stations relative to the slip patches of scenario C; (C) acceleration and velocity spectra at station 2; (D) acceleration and velocity spectra at station 3; (E) acceleration and velocity spectra at station 4

demand on the 3-story building is amplified by a factor up to 2.9 due to the presence of the slip patches, as compared to a factor of 1.6 for the FN component. The dispersion of all the parameters associated with scenarios B and C is also consistently higher than the dispersion associated with scenario A, as Figure 14 shows. This aspect is attributed to the introduction of large demands in the hybrid rupture scenarios only near the asperities, whereas the demands at locations far from the asperities (or behind the asperities in the direction of rupture) remain relatively low. These observations indicate that the aleatory variability is relatively high for ground motions generated by the hybrid rupture technique even at long distances from the fault. Although these findings are yet to be validated with a large recorded dataset of observations, this study suggests that the hybrid rupture scenarios would yield more realistic results in seismic risk assessments. Our analysis also suggests that the differences between the stochastic and hybrid rupture scenarios become significant at relatively high intensity levels; this is implied by the similar probabilities of non-exceedance for all scenarios at the distribution tails, and the widely differing probabilities at higher demand levels. For instance, at 1 km, the 12-story MIDR (Figure 14(B)) has a similar probability of not exceeding 1.5% for all scenarios (close to 25%); however, the probability of not exceeding 3.0% interstory drift is 90% for scenario A, and only 61% and 68% for scenarios B and C. This trend suggests that the presence of the high-slip patches would play an important role in determining the median collapse capacity of structures.

There is no significant difference between the dispersion in the ground motion intensity and structural demands associated with the two hybrid rupture scenarios. However, comparing the median values suggests that scenario B, on average, is somewhat more damaging than scenario C. This is visually apparent in Figure 14, which shows scenario C data points falling between those of scenario A and B for almost the entire range of probabilities. In general, the results suggest that

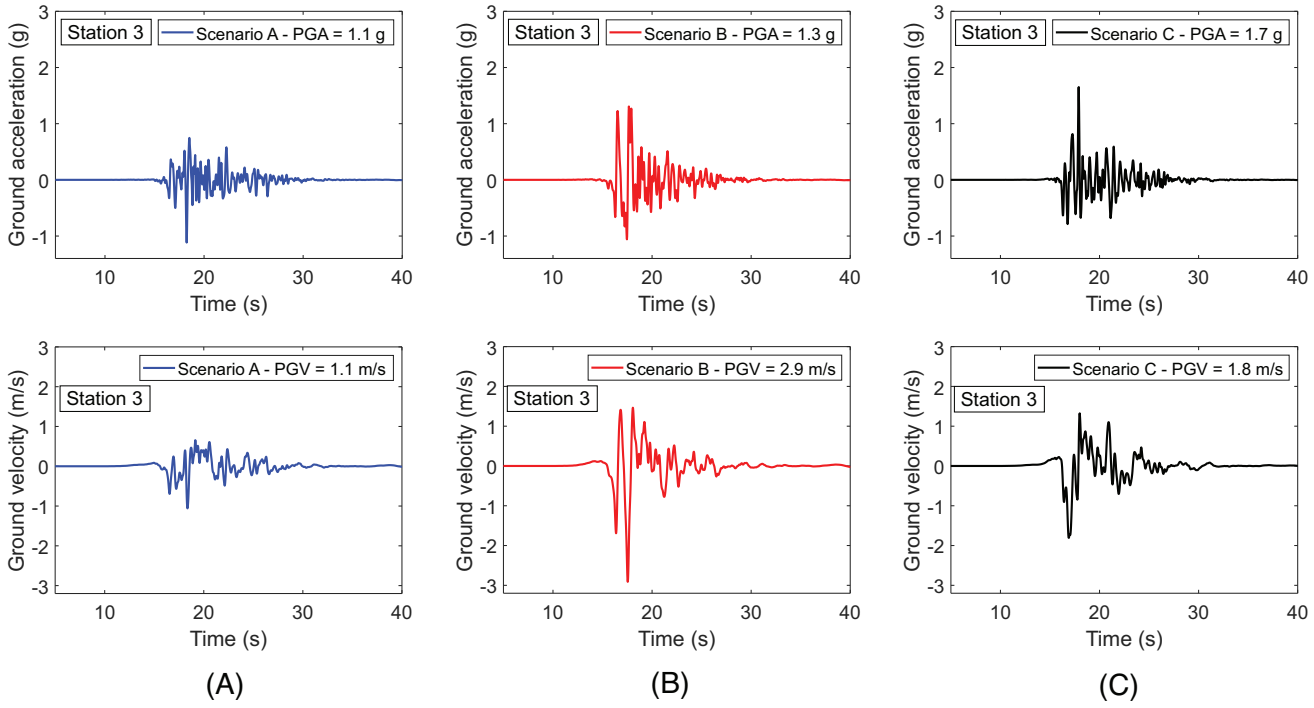

FIGURE 13 Ground acceleration and velocity time histories at station 3 for: (A) scenario A; (B) scenario B; (C) scenario C

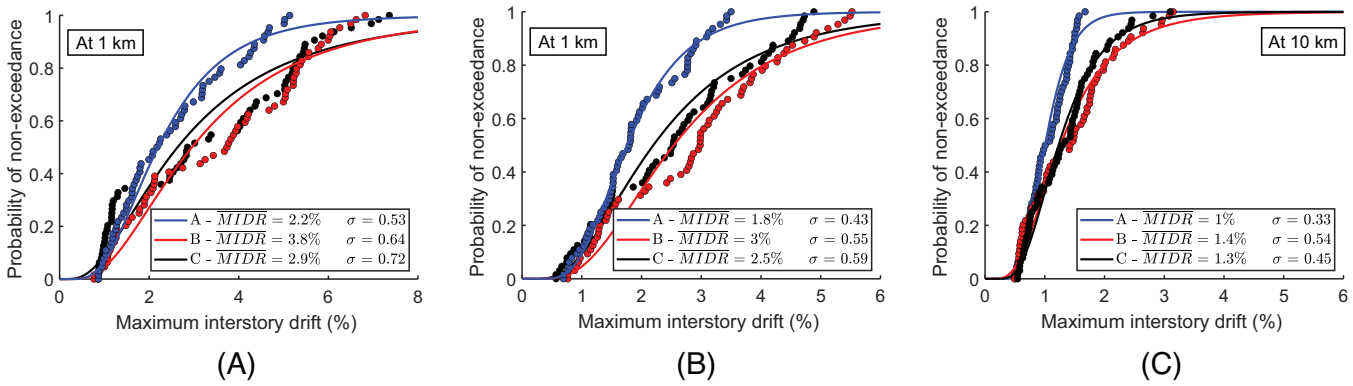

FIGURE 14 MIDR distributions along the fault in all scenarios for: (A) the 3-story building at 1 km due to the FN component; (B) the 12-story building at 1 km due to the FN component; (C) the 12-story building at 10 km due to the FP component

localized slip that is closer to the rupture initiation in a unilateral rupture would lead to higher spectral accelerations and more damaging effects to structures. Despite the large uncertainty associated with the rupture slip patterns of earthquake faults, the preceding analysis indicates that it is possible to determine locations of the rupture slip regions that provide more conservative risk estimates (among the likely scenarios based on a geophysical analysis). Confirmation of this finding necessitates further examination of the impact of the locations and size of slip patches. Nonetheless, the plots in Figure 14 indicate that a performance assessment using scenarios A and B only would not yield a substantial difference from an assessment using scenarios A, B, and C.

4.3 | Effects of the site conditions on near-fault structural response

The amplification of ground response due to focusing of the seismic energy by shallow sedimentary basins has been analyzed in a number of studies for events such as the 1994 Northridge, California, and the 1995 Kobe, Japan, earthquakes.

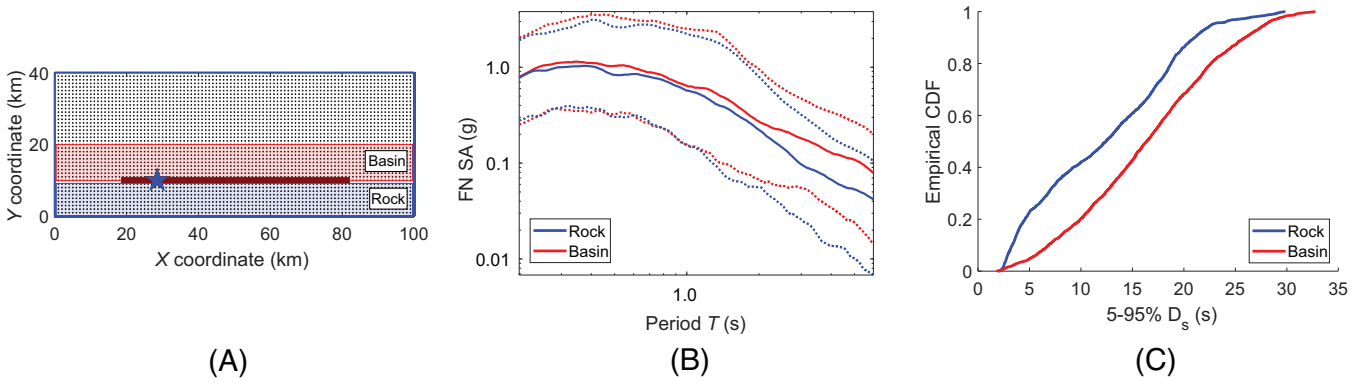

FIGURE 15 Ground motion characteristics at basin and rock sites within 10 km of the fault: (A) locations of the considered ground motions; (B) median and 2.5 and 97.5 percentile acceleration response spectra of the basin and rock datasets; (C) empirical cumulative density function of the significant shaking durations of basin and rock ground motions

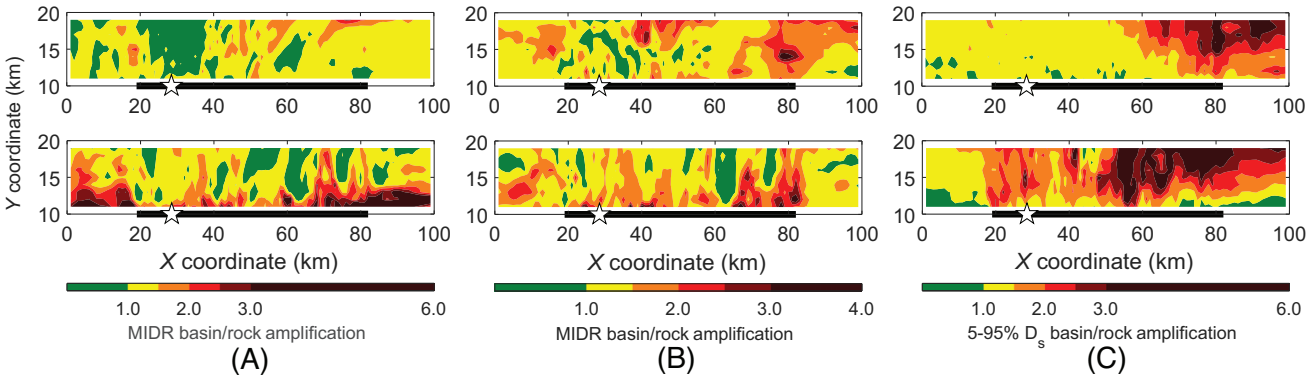

FIGURE 16 Basin amplification ratio due to the FN (upper) and FP (lower) ground motions of scenario B for: (A) the MIDR in the 3-story building; (B) the MIDR in the 12-story building; (C) the significant shaking duration

Previous studies suggested that constructive interference of the direct waves with the surface waves generated at the basin edge can significantly contribute to ground motion amplification and structural damage.[43,44] Despite the inclusion of site effects in GMPEs,[45] systematic differences due to site conditions and basin-edge effects remain difficult to characterize at short distances, because the available databases combine motions from regions all around the world. The size and geologic structure of the computational domain in this study allow for studying the differences between the ground motion waveforms at basin and rock sites of identical source distances. The ground motion characteristics were studied at stations located within 10 km of the fault (Figure 15(A)); this includes 3267 stations on the sedimentary basin side and 2673 stations on the rock side. The median acceleration response spectra and associated dispersion for both sets, plotted in Figure 15(B), demonstrate that the spectral accelerations are consistently higher on the basin side. The difference between the basin and rock ground motions is small at short periods and increases for longer periods—becoming significant for periods longer than 2 s. As a result, the structural demands near the fault are higher on the basin side for most locations, although there is significant variability in the size of the difference.

Although the main characteristics of the simulated FN and FP components are primarily controlled by the rupture directivity effects, both components are also affected by the basin edge.[43,46,47] Given the large dip angle of the basin edge, basin depth, and the fault location parallel to the edge, the near-fault ground motion is expected to be amplified in a narrow belt along the basin edge and in the frequency range 1–2 Hz.[48] To understand the variation of the ground motion amplification near the fault, maps of the basin amplification ratio of the ground motion intensity and structural demands were created for the near-fault basin area specified in Figure 15(A). The amplification ratio for a given parameter is defined as the ratio of the parameter's value at a basin site to its value at the rock site of identical source distance. Examples of such maps are shown in Figures 16(A) and 16(B) for the MIDR of both buildings due to the FN and FP components of scenario B. The maps show that the structural demand amplification near the basin edge is generally lower for the FN

component than the FP component, particularly for the high-frequency building. This observation suggests that the strong directivity effects in the FN component may dominate the response at very short-distances, such that basin and rock sites experience similar demands. In contrast, the demands due to the FP component, which is primarily free of directivity effects, experience the highest amplification very close to the basin edge. For instance, the 3-story FP MIDRs are shown to be amplified by a factor of close to 6.0 at a 1-km distance from the fault. These results point to systematic differences between the FN and FP components of motions near the fault on basin soils, which can be important for ground motion selection in engineering risk analyses.

The more severe demands imposed at basin sites are believed to be due to the combined effect of the amplified ground motion intensity and increased shaking durations. The 5–95% significant duration metric (5–95%D_s) is used in this study to assess the shaking duration. This measure represents the duration between 5% and 95% of Arias Intensity, which is computed as the integral of the square of the ground acceleration history over time ($\frac{\pi}{2g}\int_0^T a^2(t)dt$), where T is the total time of the accelerogram and g is the gravitational acceleration. The 5–95%D_s is thought to represent the duration where most of the seismic energy is released, and is seen to correlate well with structural risk.[49] The empirical cumulative distribution functions of the 5–95%D_s for basin and rock ground motions in Figure 15(C) reveal that basin sites tend to experience longer shaking durations than rock sites, which is consistent with the observations of previous studies.[43] The amplification maps in Figure 16(C) indicate that the shaking duration at near-fault basin sites is amplified significantly for both the FN and FP components (by a factor of up to 6.0). The increase in the shaking duration is found to be lowest at shorter distances and increases substantially as the distance increases (up to the 9-km distance limit of the map). Figure 16(C) also shows that the increase in the shaking duration follows different spatial patterns for the FN and FP components, implying that the strong directivity effects (which are associated with shorter durations) limit the amplification of the FN motion durations in the forward directivity zone.

To analyze the impact of the shallow basin amplification on structural response, the ground motion waveforms and structural demands were examined at several stations (Figure 17(A)) on the basin and rock sides of the domain with identical source distances. The significant duration of the FN ground acceleration increases from 5 s at station 8 to 14.7 s at station 11 (Figure 17(D)). A substantial increase is also observed in the amplitudes of the acceleration, velocity, and displacement time histories (Figures 17(D)–17(F)). Analysis of the structural response at these stations suggests that a measure of the story drifts alone may underestimate the demands imposed on the structural components at near-fault basin sites. Previous studies found that longer shaking durations impose additional loading cycles which may impact structures that are susceptible to cyclic deterioration effects, such as RC buildings.[49] The findings of this study reveal that buildings at near-fault basin sites experience higher maximum rotation demands compared to rock sites of identical source distances. The representative envelopes of the MIDR on the 12-story building in Figures 17(B) and 17(C)—along with the building plastic hinges and maximum component rotation demands—demonstrate this result: Although the maximum interstory drifts are similar for the buildings at stations 8 and 11, the building located at the basin site experiences more significant plastic hinge formation at most floors, and the maximum member rotation demand is doubled (from 12% to 25% of the hinge capacity), compared to the building at the rock site. Similarly, the maximum rotation demand at basin station 10 is 2.7 times the maximum demand at rock station 9, although the ratio between the MIDR demands at the two locations is only 1.3. The significant increase of the plasticity demands may be related to the additional energy dissipation and deterioration caused by the larger number of severe loading cycles. The results suggest that the distance-dependent shallow basin amplification effect on the intensity and shaking duration may be important for selecting ground motions in a near-fault engineering analysis, as the longer duration basin motions can substantially amplify the demands on RC structures, particularly those sensitive to the low-frequency content of the motions.

5 | CONCLUSIONS AND RECOMMENDATIONS

We utilize a suite of simulated broadband earthquake ground motions to characterize the regional-scale variation of the seismic risk to RC structures, particularly at short distances from the rupturing fault. The ground motions were generated using physics-based kinematic fault rupture models with 3D wave propagation physics for M7 strike-slip earthquakes over domains containing billions of grid points and resolved up to a frequency of 5 Hz. Over 40,000 nonlinear response history simulations were conducted on two short- and mid-rise modern RC special moment frame buildings, which were designed to satisfy modern code requirements and modeled using a methodology that incorporates nonlinear behavior and deterioration effects. The ground motion intensity and structural response quantities were studied at several distances from the rupture source for different rupture scenarios and site conditions, and the spatial and temporal variability of the

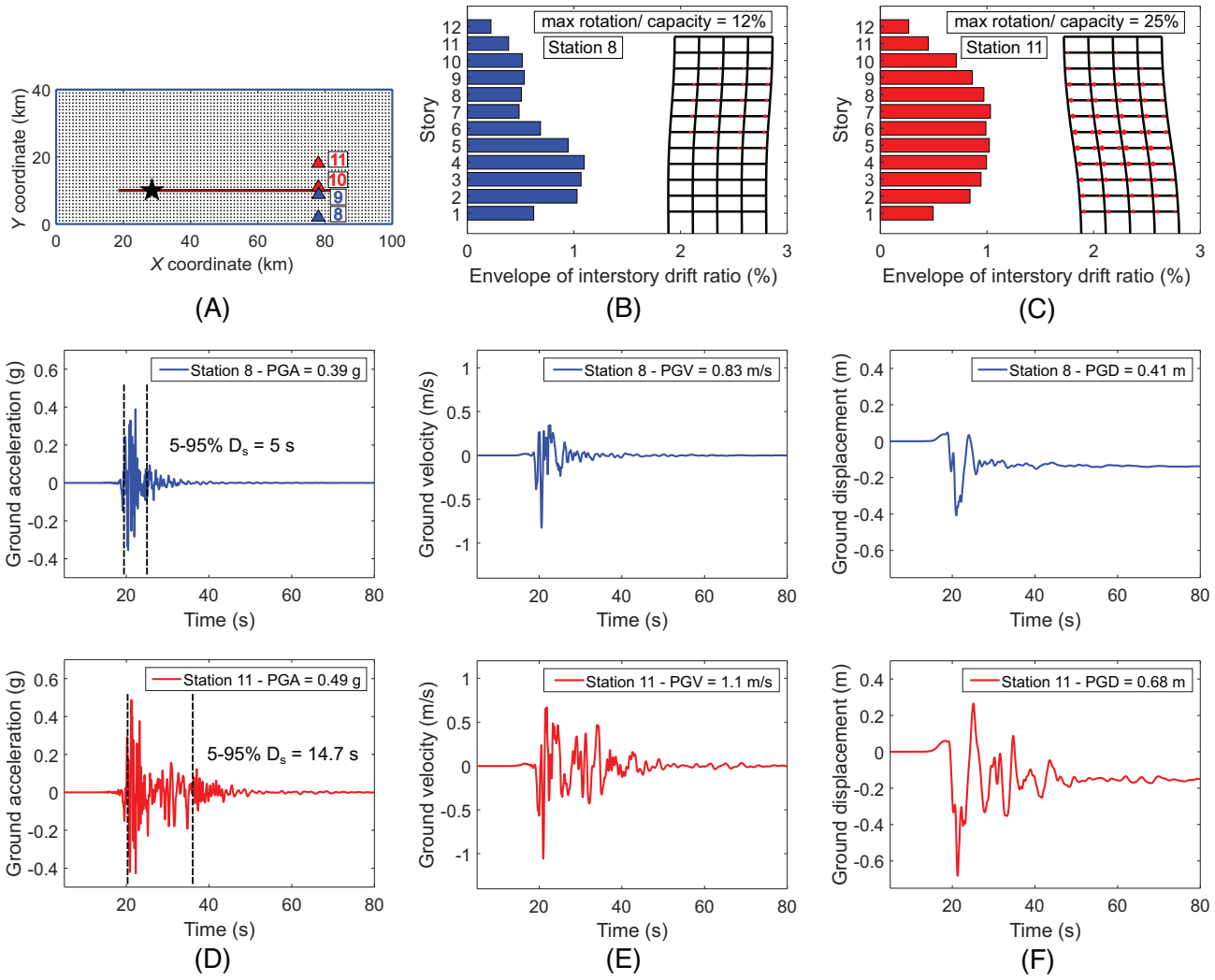

FIGURE 17 Ground motion characteristics at near-fault basin and rock sites: (A) locations of stations 8 through 11; (B) 12-story building response at station 8; (C) 12-story building response at station 11; (D) acceleration time histories at stations 8 and 11; (E) velocity time histories at stations 8 and 11; (F) displacement time histories at stations 8 and 11

expected structural demands was examined. Our analysis reveals significant spatial variability associated with the MIDR and structural member rotation demands at short distances from the fault. For short-period structures, the MIDR demands may vary by a factor of close to 8.0 at a distance of 1 km from the rupturing fault. Both the magnitudes and dispersion of the structural demands decrease significantly beyond a distance of 15 km away from the fault. The variability of the structural response is also shown to highly depend on the stiffness characteristics of the buildings, and their relationship with the frequency content of the ground motions. The response of the long-period building in this study retains a relatively wide dispersion over longer distances from the fault, as compared to the short-period building.

Our simulations show that the amplification of the ground motion components normal to the rupturing fault caused by the forward rupture directivity effect for a M7 unilateral strike-slip earthquake is predominantly concentrated within a 10-km normal distance to the fault and may lead to extreme MIDR and member rotation demands within that region. Analysis of several stations in the forward directivity path suggests that the structural demands may substantially increase as the distance forward of the rupture initiation increases up to a certain distance dependent on the rupture characteristics. Beyond that distance, the structural demands decrease significantly and the ground motions exhibit characteristics similar to far-field motions. The impacts of directivity are absent from the FP components of all motions, yet significant structural demands may be observed at longer distances, as compared to the FN components, for rupture scenarios containing deterministic high-slip regions.

The presence of localized high-slip patches along the fault consistently leads to higher ground motion intensity and structural demands over regions of the domain that are near the patches, and is associated with higher demand variability

at a given distance from the fault. The comparison between the demands induced by the stochastic rupture scenario, hybrid rupture scenarios and real records suggests that utilizing a stochastic distribution of slip alone in a seismic risk assessment may underestimate the structural demands and record-to-record variability in both near-fault and far-field locations. In addition, the locations of the largest structural demands are impacted by the locations of the rupture asperities, as is the frequency range of impact. Examining a large number of rupture scenarios with different slip patch locations and sizes is necessary to determine a best-practice sufficient number of scenarios for an engineering risk assessment. However, the preliminary findings of this study suggest that slip patches that are located closer to the rupture initiation in a unilateral rupture produce more damaging effects. The minor differences between both hybrid rupture scenarios also suggest that a small number of scenarios would likely be sufficient for an engineering risk analysis. In addition to the rupture characteristics, distance-dependent amplification of near-fault ground motion intensity and shaking duration is observed at stations proximate to the edge of the shallow basin, and leads to more significant structural demands on buildings located at basin sites—particularly flexible buildings—compared to rock sites of identical source distances. The amplified ground motions associated with basin sites can have a substantial impact on the maximum rotation demands of the structural members, which are indicators of the expected damage. Examining the ground motions near the basin edge also suggests that the FN component motions are dominated by directivity effects, and, therefore, experience less basin amplification at shorter distances, whereas the FP component intensity is significantly amplified.

The findings of this study offer important insight regarding the variability of ground shaking and structural demands for assessing the near-fault seismic risk to structures subjected to shallow crustal earthquakes, and recommendations regarding the use of simulated earthquake ground motions to conduct such assessments. Extensive parametric sensitivity studies are necessary to examine characteristics of the rupture that are not considered in this study and are expected to affect the structural demands; these include different hypocenter locations, different geometries of the rupture slip patches, varying depths to the top of the rupture, and basin edge geometry. Future studies by the authors with a larger number of scenarios will also characterize the dispersion in the structural collapse risk at a particular distance from the fault due to many possible rupture scenarios, in addition to examining the impact of the strong velocity pulses and permanent displacements (fling step) associated with near-fault ground motions on the structural risk.

ACKNOWLEDGMENTS

This research was supported by the Exascale Computing Project (ECP), Project Number: 17-SC-20-SC, a collaborative effort of two U.S. Department of Energy organizations—the Office of Science and the National Nuclear Security Administration. Arben Pitarka's work was performed under the auspices of the U.S. Department of Energy by Lawrence Livermore National Laboratory under Contract DE-AC52-07NA27344, Release: LLNL-PROC-802920. The authors gratefully acknowledge the excellent support of the National Energy Research Scientific Computing Center (NERSC) and access to the CORI computer.

ORCID


Maha Kenawy https://orcid.org/0000-0002-9722-091X

REFERENCES

1. Housner G, Trifunac M. Analysis of accelerograms-Parkfield earthquake. *Bull Seismol Soc Am*. 1967;57(6):1193-1220.
2. Bertero VV, Mahin SA, Herrera RA. Aseismic design implications of near-fault San Fernando earthquake records. *Earthq Eng Struct Dyn*. 1978;6(1):31-42.
3. Hall JF, Heaton TH, Halling MW, Wald DJ. Near-source ground motion and its effects on flexible buildings. *Earthq Spectra*. 1995;11(4):569-605.
4. Chopra AK, Chintanapakdee C. Comparing response of SDF systems to near-fault and far-fault earthquake motions in the context of spectral regions. *Earthq Eng Struct Dyn*. 2001;30(12):1769-1789.
5. Alavi B, Krawinkler H. Behavior of moment-resisting frame structures subjected to near-fault ground motions. *Earthq Eng Struct Dyn*. 2004;33(6):687-706.
6. *1997 Uniform Building Code*. International Conference of Building Officials. 1997.
7. *Minimum Design Loads and Associated Criteria for Buildings and Other Structures (ASCE/SEI 7-16)*. Reston, VA: American Society of Civil Engineers; 2017.
8. Somerville PG, Smith NF, Graves RW, Abrahamson NA. Modification of empirical strong ground motion attenuation relations to include the amplitude and duration effects of rupture directivity. *Seismol Res Lett*. 1997;68(1):199-222.
9. Abrahamson NA. Effects of rupture directivity on probabilistic seismic hazard analysis. In: Proceedings of the 6th International Conference on Seismic Zonation, Palm Springs, CA; 2000:151-156.

10. Somerville PG. Engineering characterization of near fault ground motions. In: Proceedings of, NZSEE 2005 Conference, Taupo, New Zealand; 2005.
11. Tothong P, Cornell CA, Baker J. Explicit directivity-pulse inclusion in probabilistic seismic hazard analysis. *Earthq Spectra*. 2007;23(4):867-891.
12. Douglas J, Aochi H. A survey of techniques for predicting earthquake ground motions for engineering purposes. *Surv Geophys*. 2008;29(3):187.
13. Bielak J, Loukakis K, Hisada Y, Yoshimura C. Domain reduction method for three-dimensional earthquake modeling in localized regions, Part I: Theory. *Bull Seismol Soc Am*. 2003;93(2):817-824.
14. Taborda R, Bielak J. Large-scale earthquake simulation: computational seismology and complex engineering systems. *Comput Sci Eng*. 2011;13(4):14-27.
15. Isbiliroglu Y, Taborda R, Bielak J. Coupled soil-structure interaction effects of building clusters during earthquakes. *Earthq Spectra*. 2015;31(1):463-500.
16. Jayaram N, Shome N. A statistical analysis of the response of tall buildings to recorded and simulated ground motions. In: 15th World Conference on Earthquake Engineering; 2012:1-10.
17. Burks LS, Zimmerman RB, Baker JW. Evaluation of hybrid broadband ground motion simulations for response history analysis and design. *Earthq Spectra*. 2015;31(3):1691-1710.
18. Marafi NA, Eberhard MO, Berman JW, Wirth EA, Frankel AD. Impacts of simulated M9 Cascadia subduction zone motions on idealized systems. *Earthq Spectra*. 2019;35(3):1261-1287.
19. Bijelić N, Lin T, Deierlein GG. Quantification of the influence of deep basin effects on structural collapse using SCEC CyberShake earthquake ground motion simulations. *Earthq Spectra*. 2019;35(4):1845-1864.
20. Bijelić N, Lin T, Deierlein GG. Evaluation of building collapse risk and drift demands by nonlinear structural analyses using conventional hazard analysis versus direct simulation with CyberShake seismograms. *Bull Seismol Soc Am*. 2019;109(5):1812-1828.
21. Galasso C, Zhong P, Zareian F, Iervolino I, Graves RW. Validation of ground-motion simulations for historical events using MDoF systems. *Earthq Eng Struct Dyn*. 2013;42(9):1395-1412.
22. Baker JW, Luco N, Abrahamson NA, Graves RW, Maechling PJ, Olsen KB. Engineering uses of physics-based ground motion simulations. In: Proceedings of the Tenth US Conference on Earthquake Engineering; 2014.
23. Bayless J, Abrahamson NA. Evaluation of the interperiod correlation of ground-motion simulations. *Bull Seismol Soc Am*. 2018;108(6):3413-3430.
24. Rodgers AJ, Anders Petersson N, Pitarka A, McCallen DB, Sjogreen B, Abrahamson N. Broadband (0–5 Hz) fully deterministic 3D ground-motion simulations of a magnitude 7.0 Hayward fault earthquake: comparison with empirical ground-motion models and 3D path and site effects from source normalized intensities. *Seismol Res Lett*. 2019;90(3):1268-1284.
25. Graves R, Pitarka A. Kinematic ground-motion simulations on rough faults including effects of 3D stochastic velocity perturbations. *Bull Seismol Soc Am*. 2016;106(5):2136-2153.
26. Rodgers AJ, Pitarka A, McCallen DB. The effect of fault geometry and minimum shear wavespeed on 3D ground-motion simulations for an M w 6.5 Hayward fault scenario earthquake, San Francisco Bay Area, Northern California. *Bull Seismol Soc Am*. 2019;109(4):1265-1281.
27. Mccallen D, Petersson N, Rodgers A, et al. The earthquake simulation (EQSIM) framework for physics-based fault-to-structure simulations. In: Proceedings of the 17th World Conference on Earthquake Engineering, Sendai, Japan; 2020.
28. *Building Code Requirements for Structural Concrete (ACI 318-14)*. American Concrete Institute; 2014.
29. McKenna F, Fenves GL, Scott MH, et al. *Open System for Earthquake Engineering Simulation*. Berkeley, CA: University of California; 2000.
30. Giberson MF. *The response of nonlinear multi-story structures subjected to earthquake excitation*. PhD thesis. California Institute of Technology, Pasadena, CA; 1967.
31. Ibarra LF, Medina RA, Krawinkler H. Hysteretic models that incorporate strength and stiffness deterioration. *Earthq Eng Struct Dyn*. 2005;34(12):1489-1511.
32. Haselton CB, Liel AB, Taylor-Lange SC, Deierlein GG. Calibration of model to simulate response of reinforced concrete beam-columns to collapse. *ACI Struct J*. 2016;113(6):1141-1152.
33. Sjögreen B, Petersson NA. A fourth order accurate finite difference scheme for the elastic wave equation in second order formulation. *J Sci Comput*. 2012;52(1):17-48.
34. Pitarka A, Graves R, Irikura K, Miyakoshi K, Rodgers A. Kinematic rupture modeling of ground motion from the M7 Kumamoto, Japan, earthquake. *Pure Appl Geophys*. 2019:1-23.
35. Graves R, Pitarka A. Validating ground-motion simulations on rough faults in complex 3-D media. In: Proceedings of the 11th National Conference in Earthquake Engineering, EERI, Los Angeles, CA; 2018.
36. Baker JW, Lin T, Shahi SK, Jayaram N. New ground motion selection procedures and selected motions for the PEER transportation research program. *PEER Report* 2011;3.
37. Boore DM. Orientation-independent, nongeometric-mean measures of seismic intensity from two horizontal components of motion. *Bull Seismol Soc Am*. 2010;100(4):1830-1835.
38. Somerville PG. Magnitude scaling of the near fault rupture directivity pulse. *Phys Earth Planet Inter*. 2003;137(1-4):201-212.
39. Shahi SK, Baker JW. An efficient algorithm to identify strong-velocity pulses in multicomponent ground motions. *Bull Seismol Soc Am*. 2014;104(5):2456-2466.
40. Champion C, Liel A. The effect of near-fault directivity on building seismic collapse risk. *Earthq Eng Struct Dyn*. 2012;41(10):1391-1409.

41. *Seismic Design Criteria for Structures, Systems, and Components in Nuclear Facilities (ASCE/SEI 43-05)*. Reston, VA: American Society of Civil Engineers; 2005.
42. Graves RW, Pitarka A. Broadband ground-motion simulation using a hybrid approach. *Bull Seismol Soc Am*. 2010;100(5A):2095-2123.
43. Graves RW, Pitarka A, Somerville PG. Ground-motion amplification in the Santa Monica area: Effects of shallow basin-edge structure. *Bull Seismol Soc Am*. 1998;88(5):1224-1242.
44. Pitarka A, Irikura K, Iwata T, Kagawa T. Basin structure effects in the Kobe area inferred from the modeling of ground motions from two aftershocks of the January 17, 1995, Hyogo-ken Nanbu earthquake. *J Phys Earth*. 1996;44(5):563-576.
45. Campbell KW, Bozorgnia Y. NGA-West2 ground motion model for the average horizontal components of PGA, PGV, and 5% damped linear acceleration response spectra. *Earthq Spectra*. 2014;30(3):1087-1115.
46. Kawase H. The cause of the damage belt in Kobe:"The basin-edge effect," constructive interference of the direct S-wave with the basin-induced diffracted/Rayleigh waves. *Seismol Res Lett*. 1996;67(5):25-34.
47. Pitarka A, Irikura K, Iwata T, Sekiguchi H. Three-dimensional simulation of the near-fault ground motion for the 1995 Hyogo-ken Nanbu (Kobe), Japan, earthquake. *Bull Seismol Soc Am*. 1998;88(2):428-440.
48. Pitarka A, Irikura K, Iwata T. Modelling of ground motion in the Higashinada (Kobe) area for an aftershock of the 1995 January 17 Hyogo-ken Nanbu, Japan, earthquake. *Geophys J Int*. 1997;131(2):231-239.
49. Raghunandan M, Liel AB. Effect of ground motion duration on earthquake-induced structural collapse. *Struct Saf*. 2013;41:119-133.

AUTHOR BIOGRAPHIES

Dr. Maha Kenawy is a postdoctoral scholar in the department of Civil and Environmental Engineering at the University of Nevada, Reno. Her research focuses on protecting the built environment against natural hazards. She specializes in characterizing earthquake hazard and risks to civil structures, and advancing the nonlinear modeling methods of reinforced concrete structures. Dr. Kenawy holds a Ph.D. in Civil and Environmental Engineering from the University of California, Davis, and a M.Sc. and B.Sc. in Construction Engineering from the American University in Cairo, Egypt. She is the recipient of the 2016 ASCE O.H. Ammann Research Award in Structural Engineering, and currently serves as a chair for the Younger Members Committee of the Earthquake Engineering Research Institute.

Dr. David McCallen is the Director of the Center for Civil Engineering Earthquake Research at the University of Nevada, Reno and a senior scientist at Lawrence Berkeley National Laboratory where he leads the Department of Energy EQSIM Exascale Computing Project. His career started in the Structural and Applied Mechanics Group at Lawrence Livermore National Laboratory where he developed computational software and performed advanced simulations on a number of structures. His responsibilities eventually extended to leadership of major programs including Engineering Division Leader for the National Ignition Facility, Nuclear Systems Program Leader and Deputy Principal Associate Director for Global Security. Most recently, Dr. McCallen held the position of Associate Vice President for National Laboratories in the University of California Office of the President.

Dr. Arben Pitarka is a seismologist at Lawrence Livermore National Laboratory (LLNL). He earned his PhD in Seismology from Kyoto University, Kyoto, Japan in 1997. He is the deputy Seismology Group Leader at LLNL. Before joining the LLNL he has worked as seismologist for several institutions, including the Seismological Institute in Albania, Woodward-Clyde Consultants, URS Corporation, QTSI and BAE Systems. Arben has extensive experience in computational and engineering seismology. During his career he has been the PI of several applied research projects. His current research interests include development of numerical techniques for modeling seismic sources and wave propagation, and broad-band ground motion simulation. He has made technical contributions to development and testing of numerical techniques for coupling hydrodynamic modeling of the explosion source and elastic wave propagation. His recent work is focused on dynamic earthquake rupture modeling applied to physics based strong ground motion simulation. He is the author of more than 40 peer-reviewed papers. Since 2003 he has been serving as associate editor of the BSSA.

How to cite this article: Kenawy M, McCallen D, Pitarka A. Variability of near-fault seismic risk to reinforced concrete buildings based on high-resolution physics-based ground motion simulations. *Earthquake Engng Struct Dyn*. 2021;1–21. https://doi.org/10.1002/eqe.3413